Solid State Sciences 173 (2026) 108182

Contents lists available at ScienceDirect

Solid State Sciences

journal homepage: www.elsevier.com/locate/ssscie

Electronic and thermal properties of the phase-change memory material, $Ge_2Sb_2Te_5$, and results from spatially resolved transport calculations☆

K. Nepal [a,*], A. Gautam [a], R. Hussein [a], K. Konstantinou [b], S.R. Elliott [c], C. Ugwumadu [d], D.A. Drabold [a]

[a] Department of Physics and Astronomy, Nanoscale and Quantum Phenomena Institute (NQPI), Ohio University, Athens, 45701, OH, USA
[b] Department of Mechanical and Materials Engineering, University of Turku, Turku, FI-20500, Finland
[c] Physical and Theoretical Chemistry Laboratory, Department of Chemistry, University of Oxford, Oxford, OX1 3QZ, UK
[d] Physics of Condensed Matter and Complex Systems (T-4) Group, Los Alamos National Laboratory, Los Alamos, NM, USA

ARTICLE INFO

Keywords:
Phase-change memory device
GST
Electron and thermal transport
Electron-phonon coupling
Density functional theory

ABSTRACT

We report new insights into the electronic, structural, and transport (heat and charge) properties of the phase-change memory material amorphous $Ge_2Sb_2Te_5$. Using realistic structural models of Konstantinou et al., (2019), we analyze the topology, electronic states, and lattice dynamics with density functional methods, including hybrid-functional calculations and machine-learned interatomic potentials. The Kohn–Sham orbitals near the Fermi level display a strong electron–phonon coupling, and exhibit large energy fluctuations at room temperature. The conduction tail states exhibit larger phonon-induced fluctuations than the valence tail states. To resolve transport at the atomic scale, we employ space-projected electronic conductivity and site-projected thermal conductivity methods. Local analysis of heat transport highlights the role of filamentary networks dominated by Te, with Sb and Ge making progressively smaller contributions.

1. Introduction

Germanium antimony telluride ($Ge_2Sb_2Te_5$), henceforth referred to as aGST, is fascinating and vastly studied for the science of its rapid transformation between amorphous and crystalline states and associated electrical conductivity contrast between the two states, which enables its application for practical computer memory devices.

Pioneering computer simulations of Hegedus and Elliott [1] revealed that it is possible to study the nature of the phase change quite directly from accurate molecular dynamics (MD) simulations. A vast amount of insight has accrued from this beginning [2–9].

In this paper, we utilize realistic computer models of amorphous aGST (henceforth referred to as aGST) due to Konstantinou, Mocanu, Lee, and Elliott (KMLE) [7] to explore electronic structure and dynamics using a hybrid functional, and we compute quantities of technological interest, including spatially local estimates of charge and heat transport in the materials. We include three Appendices which offer a short, self-contained description of the transport methods. Details on the transport calculations may be found in the original papers [10–13].

The principal conclusions of this work are that (i) there are large thermally induced fluctuations of Kohn–Sham states near the Fermi level, highlighting the importance of electron–phonon coupling in electronic conductivity, (ii) electronic conductivity is spatially heterogeneous and often involves Sb-vacancy environments, and (iii) site-projected thermal conductivity analysis shows that Te- and Sb-rich regions preferentially contribute to heat transport. Together, these findings establish that electronic and thermal transport in aGST are spatially inhomogeneous, significantly influenced by phonons, defect-sensitive, and governed by a small subset of structurally distinct motifs - insights that may provide information for tailoring phase-change memory materials at the atomic scale.

The remainder of the paper is organized as follows. Section 2 describes the computational methodology, including model construction (relaxation), electronic-structure calculations, and vibrational analysis. We compute estimates of spatially resolved transport: Space-projected conductivity (SPC) and site-projected thermal conductivity (SPTC). We provide concise descriptions of these methods in Appendices A.1 and A.3, respectively. Section 3 presents the structural changes of the KMLE models under HSE06 relaxation, associated electronic structure, and defects. We investigate thermally driven electronic fluctuations near the Fermi level, and report spatially resolved electronic and thermal transport. Section 4 summarizes our findings and discusses broader implications for phase-change memory design. In the representation of

☆ This article is part of a Special issue entitled: 'Computational modelling of materials' published in Solid State Sciences.

* Corresponding author.
E-mail addresses: kn478619@ohio.edu (K. Nepal), cugwumadu@lanl.gov (C. Ugwumadu), drabold@ohio.edu (D.A. Drabold).

https://doi.org/10.1016/j.solidstatesciences.2025.108182
Received 3 October 2025; Received in revised form 6 December 2025; Accepted 10 December 2025
Available online 15 December 2025

atoms in the figures in this work, Ge, Sb, and Te are colored teal, purple, and brown, respectively.

2. Methodology

2.1. aGST structural models

Computations described in this paper used the *ab initio* plane wave code Vienna Ab initio Simulation Package (VASP) [14]. Twelve cubic supercells of aGST containing 315 atoms with chemical composition germanium (Ge), antimony (Sb), and tellurium (Te) in a 2:2:5 ratio due to KMLE [7] were considered in this work. We also used a 900-atom aGST model as well. These models are referred to as M1, M2, ..., and M12 for the rest of the paper. These aGST models were initially generated through classical molecular dynamics simulations, implemented in LAMMPS (Large-scale Atomic/Molecular Massively Parallel Simulator) [15] employing a machine-learned Gaussian approximation potential (GAP) developed by Mocanu et al. [16].

2.2. Topological and electronic structure

To accurately compute the electronic structure and gap states near the Fermi level (ε_f), we carried out relaxations and electronic structure calculations using the hybrid functional of Heyd, Scuseria, and Ernzerhof (HSE06) [17]. The thermal MD performed in this work also used HSE06. Periodic boundary conditions were used in all calculations. A plane-wave basis set with a kinetic energy cut-off of 240 eV for geometrical relaxation was used. A kinetic energy cut-off of 520 eV was implemented for electronic structure calculation. The Brillouin zone of the supercell models was sampled at the Γ point.

2.2.1. Spatially local estimates of transport

Electronic and thermal transport are determined by the network topology, chemical order, electronic, and vibrational properties of materials. For a disordered system, no two sites are identical, and it is unknown how much variation exists from site to site. For purposes of engineering materials with preferred transport properties, atomic-level insights may be helpful.

For both the thermal and electronic case we have made two assumptions: (1) the validity of a Kubo formula (either the Kubo–Greenwood Formula (KGF) or the Green-Kubo Formula (GKF) [18,19]), and assumptions implicit to these (thermal equilibrium, linear response, and an expression for the heat or electron current) and (2) a spatial decomposition of the Kubo formula to provide local information about either form of transport. Our innovation here has involved only the second point and the formulation and interpretation of the electronic and thermal conductivity are discussed in Appendices A.1 and A.3, respectively.

2.3. Vibrational properties

The vibrational signatures of the aGST models were examined by computing the vibrational density of states (VDOS) and vibrational inverse participation ratio (VIPR) within the harmonic approximation (HO). The dynamic matrix (DM) was constructed from finite differences from the usual definition:

$$D_{ij}^{\alpha\beta} = \frac{1}{\sqrt{m_i m_j}} \frac{\partial^2 E}{\partial u_i^\alpha \partial u_j^\beta} \tag{1}$$

Here, u_i^α is the small displacement of ith atom along cartesian (α) direction, m_i is the mass of the ith atom, and E is the potential energy. The eigenvalue problem for the classical normal modes at the center ($\mathbf{k} = \mathbf{0}$) of the phonon Brillouin zone is [12]:

$$\omega_m^2 \; e_i^{\alpha,m} = \sum_{\beta j} D_{ij}^{\alpha\beta} e_j^{\beta,m} \tag{2}$$

where, ω_m and e_i^α are the vibrational frequency of the mode m and sets of displacement directions for each atom in the mode m at atom i along the α direction. The Vibrational Inverse Participation Ratio (VIPR) (g) corresponding to the vibrational modes m are:

$$g(m) = \frac{\sum_{i,\alpha} |e_i^{\alpha,m}|^4}{\left(\sum_{i,\alpha} |e_i^{\alpha,m}|^2\right)^2} \tag{3}$$

VIPR is a measure of localization, and varies between 1/N (extended vibrational mode) and 1 (ideally localized vibrational mode). To compute the DM, defined in Eq. (1), each atom in aGST was displaced 0.05 Å in x-, y-, and z-directions, from its energy-minimized configuration. The resulting modes were also employed to calculate the thermal conductivity and site-projected thermal conductivity.

3. Results

3.1. Structural relaxation

In this section, we report the change in coordination in the aGST models due to relaxation with HSE06. A radial cut-off distance of 3.2 Å was used to define coordination. Fig. 1 illustrates the average coordination of atomic species before and after HSE06 relaxation in red and blue histograms, respectively. Before relaxation, it is observed that Ge prefers three- and four-fold coordination, while Sb favors three- and two-fold coordination, and Te favors three- and two-fold coordination, as shown by the red histograms in Fig. 1. Following relaxation, the basic features remain unchanged; however, a reduction in three-fold coordination in Ge and Sb was observed with an increase in four- and five-fold coordination environments, which suggests formation of defective octahedral motifs. This is supported by the Ge-centered and Sb-centered angle distribution, which shows a pronounced increase around ≈170°, confirming that the higher coordination arises from these distorted octahedral environments [20], see Figure S1. For Te, increased three- and four-fold coordination was observed with reduced two-fold coordination. The findings are shown respectively as blue and red histograms in Fig. 1.

3.2. Defects in aGST

The electronic structure of the models is sensitive to the choice of exchange–correlation functional and pseudopotential within density functional theory (DFT) [5,21]. All models were relaxed and analyzed using the HSE06 functional. KMLE [7,9] used a similar hybrid-functional calculation to examine electronic structure. Here, we report the relatively minor changes in structure resulting from HSE06, and also carry out computationally demanding thermal molecular dynamics (MD) simulations with HSE06.

The electronic structure nomenclature is defined by four categories: clean gap, shallow gap, mid-gap, and multiple mid-gap. Of the twelve models, five have gap states. Of the five models with gap states, three have a shallow gap state near the conduction band edge, three models have one mid-gap state, and one model has two mid-gap states. Where electronic structure is concerned, the only difference between this work from KMLE involved M4, which showed no mid-gap state.

The band gap in an amorphous material is usually described as the Mott or mobility gap, E_{gap}, which is the energy splitting between the extended electronic state at the conduction mobility edge (CME; E_{edge}^C) and the valence mobility edges (VME; E_{edge}^V):

$$E_{gap} = E_{edge}^C - E_{edge}^V \tag{4}$$

E_{edge}^C (E_{edge}^V) is the lowest (highest) energy extended state in the conduction (valence) band.

To estimate the localization of electronic states, we computed the electronic inverse participation ratio (IPR) and define states with IPR < 0.1 as extended states. The mobility gaps range from 0.66–0.87 eV

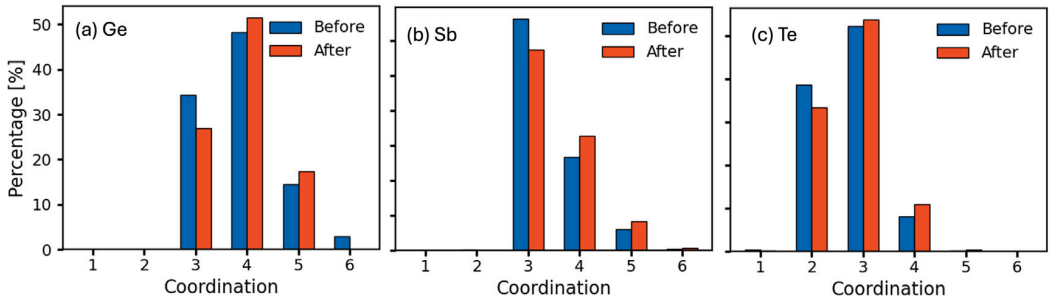

Fig. 1. Coordination analysis for the local environment of (a) germanium, (b) antimony, and (c) tellurium, respectively, averaged over twelve aGST models from KMLE after HSE06 relaxation (Red color). Coordination number was calculated by using a cut-off bond distance of 3.2 Å for each atom species. The blue histogram shows the average coordination calculated from before HSE06 relaxation.

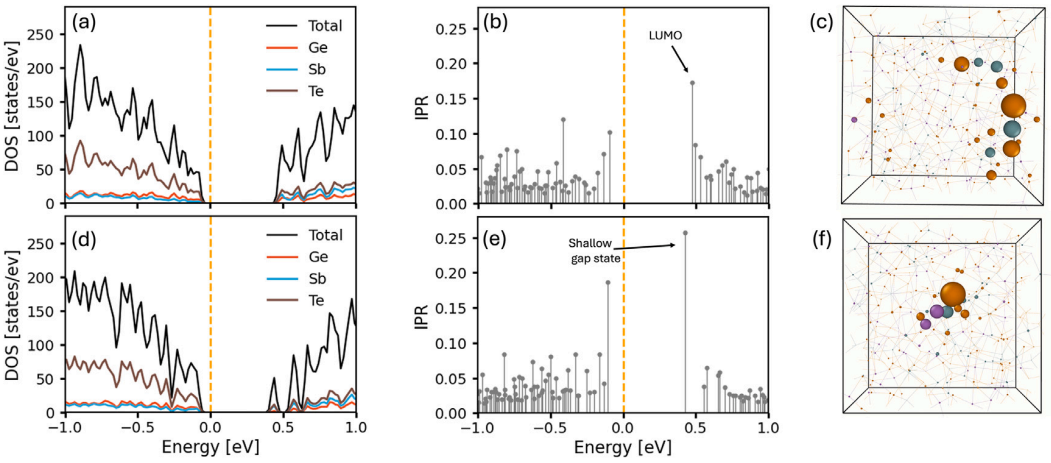

Fig. 2. (a) The total and projected density of states near the band edges for M3. The projected density of states for atomic species reveals that Te dominates the band edges. (b) The IPR indicates the extent of electronic localization of states near the band edges. (c) Atom-projection of the states at the conduction band edge, LUMO, labeled in (b). The conduction tail state is predominantly due to Ge–Te and Ge–Ge, Te–Te forming a network illustrated by a large sphere. The volume of the sphere represents the atomic contribution to the conduction band tail state. (d) The total and projected density of states near the band edges for M7 show a shallow-gap defect near the conduction band edge. (e) The shallow gap state is localized (IPR ≈ 0.25). (f) Atom-projection of the shallow gap state is predominantly due to a Te atom (the largest brown sphere in (f)), and Sb–Sb bonds. The yellow vertical dashed lines in Figure (a–d) represent the Fermi level, shifted to 0. Color code: teal - Ge, purple - Sb, and brown - Te.

with an average mobility gap of 0.76 eV (tabulated in Table 1) in reasonable agreement with other simulations [7,22] which report values between 0.5–0.8 eV and experimental values (>0.7 eV) [23,24]. The positions of defect states (mid-gap and shallow-gap) with respect to the CME are tabulated in Table 1.

3.2.1. Clean gap aGST model

Seven out of twelve aGST models exhibit a clean gap in the electronic density of states. A representation using M3 in Fig. 2a, where the vertical dashed line is a Fermi energy (shifted to 0 eV). The electronic inverse participation ratio (IPR) gauges electronic localization, analogous to VIPR defined above.[1] The valence band tail is mostly derived from Te atoms, whereas all the atomic species contribute to the conduction band tail. The IPR is indicated by gray vertical lines in Fig. 2b. States near the conduction band minimum and valence band maximum are significantly localized. The atomic projection of a conduction band tail state (LUMO), labeled "i" in Fig. 2b, shows a contribution from a chain of Ge and Te atoms forming a filament of length ≈9 atoms. Such filamentary motifs are consistent with prior reports that near-linear Te–Ge–Te units act as favorable sites for electron localization in the conduction band tail [26]. This is illustrated in Fig. 2c, where the size of the sphere represents the weights of the atom to the LUMO.

3.2.2. Shallow-gap defect aGST model

Three aGST models (M7, M8, and M9) exhibited a shallow-donor level near the conduction edge. The shallow defect levels are 0.12–0.15 eV below the CME, which is slightly lower than the experimentally reported value of 0.18 eV [27], and KMLE. The total and projected density of states for the M7 model is shown in Fig. 2d, showing a shallow donor state at ≈0.13 eV below the CBM. The level is localized, as indicated by the high IPR value in Fig. 2e. Projection of the shallow-gap defect state onto atomic species reveals localization primarily on a cluster of atoms formed by Te atoms and neighboring Sb–Sb and Te–Te homopolar bonds, as illustrated in Fig. 2f. The size of the sphere in Fig. 2f corresponds to the weight of the contribution by the atom to the shallow gap. Similar shallow defects have previously been attributed to homopolar bonding [9].

[1] This is carried out rather crudely in this paper, using the atom-projected atomic orbitals from VASP. It would be preferable to apply a more sophisticated method like LOBSTER [25].

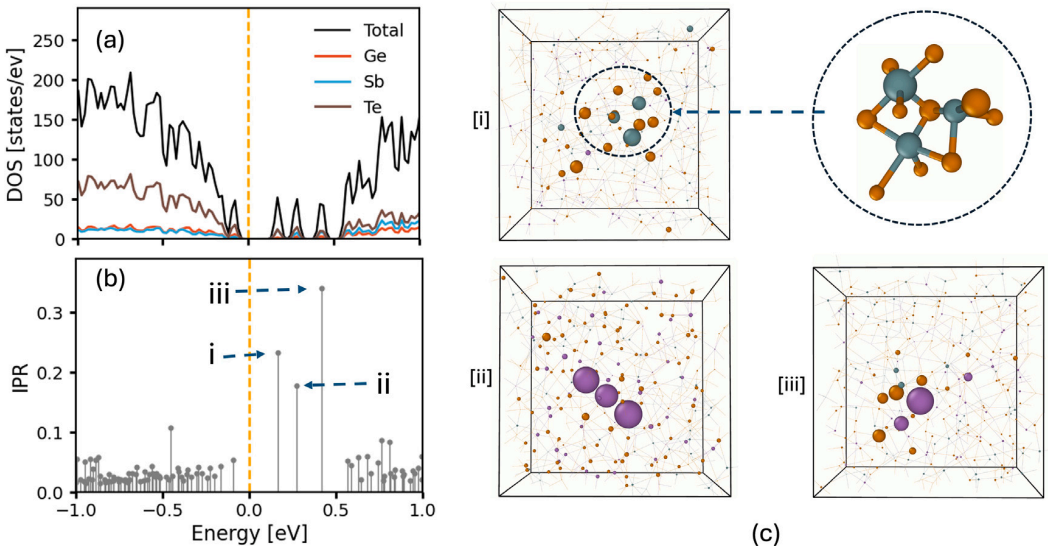

Fig. 3. (a) The total and projected density of states near the band edges for the aGST model M8 shows multiple defects in the mobility gap. (b) Mid-gap states ("i–ii") and a shallow-gap defect ("iii") are localized, indicated by high IPR values. (c) [i–iii] Atom-projection of the mid-gap states and a shallow-gap state. The mid-gap state "i" is predominantly due to a cluster of over-coordinated Ge atoms with Te atoms (cluster is highlighted). Second mid-gap state "ii" 0.30 eV below the conduction mobility edge is localized on a Sb–Sb–Sb trimer structure, while shallow-defect state "iii" 0.15 eV below the conduction mobility edge is centered at a group of Sb and Te atoms, shown in (c) [ii–iii], respectively. The volume of the sphere in (c) indicates the weight of atomic contributions to the defect state. The yellow vertical dashed lines in Figure (a–b) represent the Fermi level, shifted to 0. Color code: teal - Ge, purple - Sb, and brown - Te.

Table 1
Mobility gap, mid-gap and shallow-gap states for the twelve models.

Model	Mobility gap (eV)	Mid-gap (eV)[a]	Shallow-gap (eV)[a]
M1	0.81	–	–
M2	0.70	0.37	–
M3	0.66	–	–
M4	0.79	–	–
M5	0.84	0.44	–
M6	0.82	–	–
M7	0.69	–	0.13
M8	0.68	0.40, 0.30	0.15
M9	0.72	0.31	0.12
M10	0.87	–	–
M11	0.73	–	–
M12	0.86	–	–

[a] Energies are reported as offsets below the CME (i.e., deeper into the gap toward the Fermi level). Mean mobility gap across models: 0.76 ± 0.08 eV.

3.2.3. Mid-gap defect aGST model

Three aGST models (M2, M5, and M9) exhibit a mid-gap defect deep in the band gap. The total density of states for model M5 is shown in Figure S2a. The projection of the defect state into atomic contributions revealed that over-coordinated Ge atoms are responsible for these deep defects: see Figure S2b, where the size of the sphere shows the weight of the atom species to the mid-gap state. The structural motif of these Ge atoms is the local crystal-like bonding environment in the amorphous network (see Figure S2c), where the Ge atom is responsible for the state in a rock-salt environment. This observation has previously been reported by Ref. [7]. Ref. [7] also demonstrated that these mid-gap defects are capable of creating deep electron traps within the band gap.

3.2.4. Multiple mid-gap defect aGST model

One aGST model, M8, exhibits two mid-gap states. The electronic density of states for M8 is shown in Fig. 3a, showing two mid-gap defects at 0.40 and 0.30 eV below the conduction mobility edge. An additional shallow defect level was observed at 0.15 eV below the conduction mobility edge. These defect states are localized as illustrated by the high vertical line for the IPR in Fig. 3b. To study the structural motif of these gap defects, each state, labeled "i–iii", is projected onto atomic species, as shown in Fig. 3c[i–iii], respectively, where the size of the sphere indicates the weight of the atoms contributing to the defect states. The projection shows that a cluster involving over-coordinated Ge atoms contributes to the mid-gap state 0.40 eV below the CME. The local structure of the cluster is highlighted as a magnified image in Fig. 3c[i]. Two five-fold and one four-fold Ge atoms bonded to Te atoms contribute to the mid-gap defect. The projection of the mid-gap state, labeled "ii", onto atomic species shows that the state is localized in a Sb–Sb–Sb bond network; see Fig. 3c[ii], while a group of Sb and Te atoms contributes the most to the shallow defect state "iii", see Fig. 3c[iii].

3.3. Electron–phonon coupling and conductivity

The electron–phonon coupling is large for localized states [28,29], and this has implications to charge transport. This is related to Thomas' concept of phonon-induced delocalization [30,31]. Thomas' view is justified by time-dependent DFT calculations in amorphous silicon (a-Si) [32,33]. It seems likely that the effect is relevant in aGST.

Within an adiabatic approximation [34,35], we discuss thermally induced fluctuations in the states around the Fermi level, considering the aGST model M5 with a single mid-gap defect. Model M5 is thermally equilibrated at room temperature (300 K) for 1.3 ps using the HSE06 functional with Nosé–Hoover thermostat [36,37] at a time step of 1.5 fs. Refer to Figure S3a for the average root-mean-square deviation (RMSD) of each atomic species. Significant fluctuation of the mid-gap and higher energy levels at the conduction band edge, over time, were observed. The position of this mid-gap state fluctuates $\approx\pm$ 0.17 eV around the mean energy level, as illustrated by the yellow plot in Fig. 4a. States above ε_f fluctuate more than valence tail states, a situation also seen in a-Si [38].

For the first five states above ε_f, the RMS fluctuation is correlated with localization — higher localization, more fluctuation. The pattern is less clear for states at or below the Fermi level, which uniformly show less fluctuation than low-lying conduction levels (see Fig. 4b). The reason for this is uncertain, though probably connected to the fact that

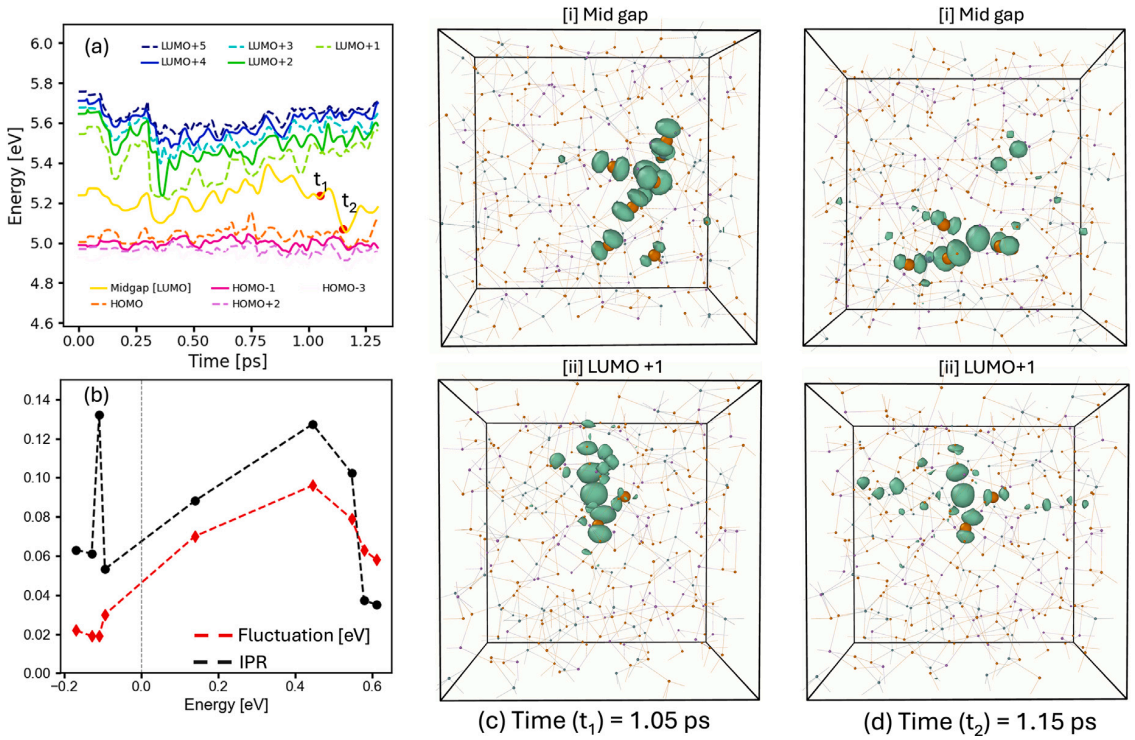

Fig. 4. All plots correspond to M5 thermally equilibrated at 300 K using a Nosé-Hoover thermostat with a time step of 1.5 fs. (a) Fluctuation in Kohn–Sham orbitals near the Fermi level, depicting fluctuations in mid-gap (solid yellow). See legends for fluctuations in different orbitals. (b) Energy-resolved orbital properties for selected states in the aGST model M5. Black markers and lines show the inverse participation ratio (IPR), indicating the degree of localization of each state. The red dashed line with diamond markers represents the thermal fluctuation of the corresponding orbital energies. (c–d) Snapshots of mid-gap(LUMO) and LUMO+1 energy level as an isosurface plot at times "t_1" and "t_2", respectively, labeled in (a).

Table 2
Atomic species resolved statistics for all 12 aGST models, showing the minimum (ζ_{min}), mean ($\langle\zeta\rangle_i$, with standard deviation, σ_ζ), maximum (ζ_{max}) values, as well as per-element thermal conductivity (κ_i). The "Avg." row shows the average value per column.

Model	Ge [$\times10^{-3}$ W/m K]				Sb [$\times10^{-3}$ W/m K]				Te [$\times10^{-3}$ W/m K]			
	ζ_{min}	$\langle\zeta\rangle_{Ge}$ (σ_ζ)	ζ_{max}	κ_{Ge}	ζ_{min}	$\langle\zeta\rangle_{Sb}$ (σ_ζ)	ζ_{max}	κ_{Sb}	ζ_{min}	$\langle\zeta\rangle_{Te}$ (σ_ζ)	ζ_{max}	κ_{Te}
M1	0.21	0.41 (0.11)	0.80	28.9	0.22	0.46 (0.11)	0.72	32.5	0.26	0.52 (0.12)	0.87	91.4
M2	0.24	0.42 (0.09)	0.65	29.3	0.23	0.47 (0.12)	0.96	32.7	0.25	0.50 (0.10)	0.85	87.0
M3	0.19	0.40 (0.12)	0.69	28.2	0.26	0.47 (0.11)	0.88	33.0	0.30	0.51 (0.10)	0.84	89.4
M4	0.21	0.41 (0.10)	0.75	28.7	0.23	0.48 (0.12)	0.82	33.7	0.23	0.51 (0.10)	0.79	88.6
M5	0.25	0.41 (0.09)	0.65	29.0	0.25	0.49 (0.10)	0.71	34.0	0.23	0.53 (0.11)	0.86	92.5
M6	0.22	0.42 (0.08)	0.60	29.3	0.26	0.47 (0.09)	0.67	32.9	0.29	0.50 (0.09)	0.83	86.9
M7	0.15	0.38 (0.09)	0.65	26.3	0.23	0.45 (0.08)	0.65	31.6	0.28	0.51 (0.10)	0.84	90.0
M8	0.24	0.42 (0.10)	0.63	29.6	0.30	0.50 (0.08)	0.69	34.7	0.28	0.54 (0.12)	0.95	95.0
M9	0.24	0.41 (0.08)	0.60	28.7	0.29	0.45 (0.10)	0.65	31.2	0.16	0.51 (0.10)	0.77	88.9
M10	0.12	0.43 (0.21)	1.30	30.4	0.04	0.48 (0.18)	0.90	33.7	0.01	0.55 (0.24)	2.13	96.5
M11	0.25	0.43 (0.10)	0.72	30.1	0.24	0.47 (0.10)	0.73	33.2	0.30	0.52 (0.10)	0.80	91.8
M12	0.15	0.42 (0.10)	0.64	29.2	0.27	0.48 (0.10)	0.80	33.5	0.28	0.53 (0.11)	0.87	92.7
Avg.	0.21	0.41 (0.10)	0.72	29.0	0.24	0.47 (0.11)	0.77	33.1	0.24	0.52 (0.11)	0.95	90.9

valence states contribute Hellman-Feynman forces to the ions, whereas the states above ε_f do not.

These calculations suggest that the band tails of aGST, especially the conduction tail, might exhibit a significant temperature dependence [38]. Perhaps this could be experimentally probed using total photoelectron yield spectroscopy (for the case of amorphous silicon, see the work of Aljishi et al. [39]). A T-dependent conductivity can be estimated using a thermally averaged version of the N^2 method [40], briefly reiterated in Appendix A.2.

We present snapshots of Kohn–Sham orbitals at selected time steps to illustrate the evolution of two higher energy states above the ε_f: (i) a mid-gap level (LUMO) and (ii) a LUMO+1. Two representative times, labeled t_1 and t_2 (taken 100 fs apart), are marked by red dots in the mid-gap level plot in Fig. 4(a). During this interval, the mid-gap level shows pronounced fluctuations compared to LUMO+1. The Kohn–Sham orbital snapshots at these times are shown in Fig. 4c and d. The eigenvectors, visualized as green isosurface plots, corresponding to the mid-gap level, reveal two distinct chain-like networks within the system, while the LUMO+1 shows a minor change in the structural network. Importantly, the localized Kohn–Sham orbitals (mid-gap and LUMO+1) exhibit large thermally induced fluctuations, leading to substantial variations in instantaneous charge density. We further observe that the eigenvectors of the mid-gap level arise from networks centered on overcoordinated Ge atoms.

The influence of electron–phonon interaction on electronic conductivity is examined via SPC analysis (see Appendix A.1), obtained at different snapshots along a thermal MD trajectory. The wave-functions

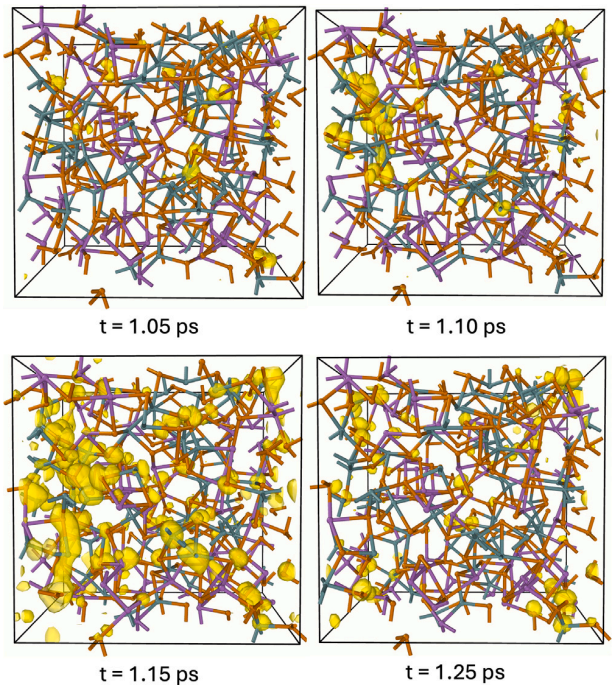

Fig. 5. Thermally driven electronic conductivity fluctuations for M5 at 300 K. The SPC isosurface plot reveals fluctuations in conduction-active regions in the model at different times. Color code: teal -Ge, purple - Sb, and brown - Te.

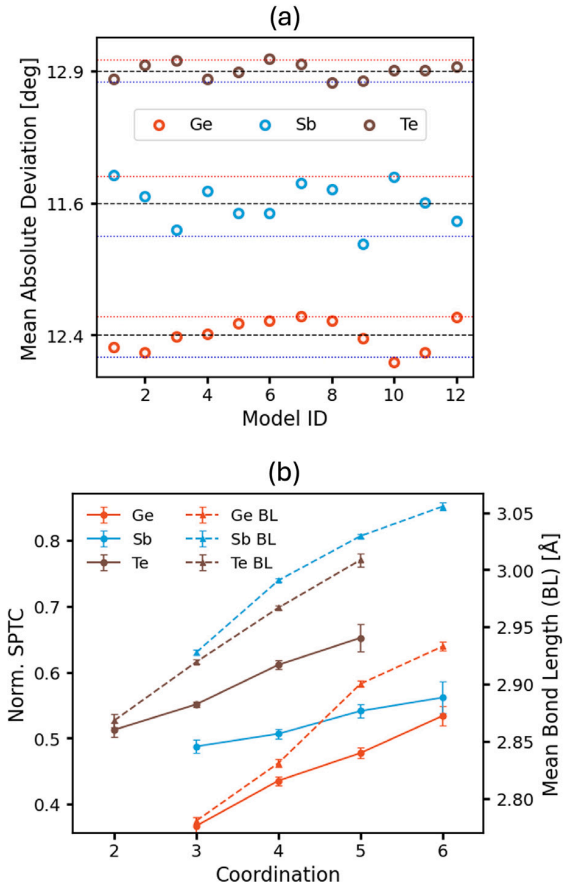

Fig. 6. Thermal transport character in aGST. (a) Mean absolute deviation (MAD) from rock-salt three-body angles (90° between two adjacent ions in the octahedron's equatorial plane) for each centered element. The blue and red dotted lines represent the 5th (blue) and 95th (red) percentiles of the distribution. (b) Correlation between (normalized) SPTC, bond length (BL), and coordination number per species averaged for models M1 to M12.

in Eq. (A.1) are the Kohn–Sham orbitals $\Psi_{i,\mathbf{k}}$ computed within VASP. The partial occupancies of the energy levels near the Fermi level were approximated using the electronic temperature $T = 1000$ K for the Fermi-Dirac distribution, which enables a reasonable sampling of Kohn–Sham states near the Fermi level. This is admittedly artificially large and invoked due to the sparse sampling of energy levels near the gap, an intrinsic limitation for our small models.

Six snapshots, spaced 75 fs apart, sampled from the final 1.3 ps of the 300 K MD simulation, were selected for SPC computations. The electronic conductivity spans a wide range, from 10^{-5} to 10^{-1} S/cm. Although the Kubo–Greenwood formula predicts average conductivities comparable to experimental reports (≈10^{-3} S/cm [41]), the large variability among snapshots reflects fluctuations in the mobility gap and in the localization of states near the Fermi level. The mobility gap fluctuates significantly around ≈0.57 ± 0.09 eV (see Figure S3b). The SPC for four of the snapshots is shown in Fig. 5, illustrating how conduction-active regions evolve with lattice vibrations. SPC depicts the fluctuation in electronic conductivity that evolves from a low-conducting state (at times 1.05 ps and 1.10 ps) to a comparatively higher conducting state (at 1.15 ps) and reverts to a poor-conducting state (at time 1.25 ps). Refer to Figure S4 for the atomic species contribution to the SPC.

3.4. Thermal transport in aGST

Site-projected thermal conductivity evaluations were conducted at room temperature (300 K) for the aGST models. The SPTC extracted for the aGST models in Table 2 and mirrored in Figure S5a (Ge), S5b (Sb), and S5c (Te), indicates systematic species ordering, $\langle\zeta\rangle_{\mathrm{Te}} > \langle\zeta\rangle_{\mathrm{Sb}} > \langle\zeta\rangle_{\mathrm{Ge}}$, across nearly all structures. From the "Avg." row, the mean values are 0.52 × 10^{-3} W/m K (Te), 0.47 × 10^{-3} W/m K (Sb), and 0.41 × 10^{-3} W/m K (Ge); thus Te carries, on average, ≈11 × 10^{-5} W/m K absolute more SPTC than Ge (≈27% higher) and ≈5 × 10^{-5} W/m K more than Sb (≈11% higher). The reported intra-species dispersions are comparable (mean $\sigma_\zeta \approx 1\text{–}1.1 \times 10^{-4}$ W/m K), giving coefficients of variation[2] clustered near 0.24 (Ge), 0.23 (Sb), and 0.21 (Te)–typical for amorphous chalcogenides with heterogeneous local environments [42,43].

The extrema ($\zeta_{\max}$) further reinforce this hierarchy with the average of per-model κ maxima being 0.95 × 10^{-3} W/m K for Te versus 0.77 × 10^{-3} W/m K for Sb and 0.72 × 10^{-3} W/m K for Ge (also see Figure S5 a, b, and c). The element-averaged κ mirror the same pattern: $\kappa_{\mathrm{Te}} \approx 0.091$ W/m K, about three times κ_{Sb} (≈0.033 W/m K) and κ_{Ge} (≈0.029 W/m K). For 900-atom aGST, we computed $\kappa_{\mathrm{Te}} \approx 0.092$ W/m K, $\kappa_{\mathrm{Ge}} \approx 0.030$ W/m K, $\kappa_{\mathrm{Sb}} \approx 0.033$ W/m K showing the modest role of finite-size on the thermal conductivity. Of course, the Te carries more heat than the other species from the stoichiometry of the material.

Evaluating its predictive performance at room temperature, we find an average thermal conductivity of 0.15 W/m K across the twelve aGST models, in good agreement with the experimental room temperature value of ≈0.20 W/m K [44], as well as theoretical values (0.15–0.2 W/m K) [45,46]. The delta function in Eq. (A.13) is approximated by a Lorentzian function with the smearing parameter 2 K (in units of

[2] Coefficient of variation is the ratio to standard deviation to the mean.

Table 3
Mode-resolved thermal conductivity of models M5 and 900-atom GST at room temperature.

Modes	Thermal conductivity (W/m K)	
	M5	aGST-900
Propagons	0.009 [~5%]	0.006 [~4%]
Diffusons	0.152 [>94%]	0.150 [>95%]
Locons	0.001 [<1%]	0.001 [<1%]

temperature), refer to Appendix A.3.1 for discussion on the broadening factor and thermal conductivity.

SPTC variance outliers highlight the structural sensitivity of aGST. Model M10, in particular, shows the broadest intra-species spreads (Te: $\sigma_\zeta = 0.24$; Ge: $\sigma_\zeta = 0.21$; Sb: $\sigma_\zeta = 0.18$), reflecting a highly heterogeneous transport landscape. The angular metrics in Fig. 6(a) provide a structural explanation: larger deviations from the ideal aGST rock-salt three-body angle [47,48] correlate with suppressed SPTC, and it is characteristic of angles in defective octahedral motifs [8]. The black lines mark the mean angular deviations (MAD) of 11.6°, 12.4°, and 12.9° for Sb, Ge, and Te, respectively (see Table S1). The lower (blue) and upper (red) dashed lines indicate the 5th and 95th percentiles of the distributions, so atoms near the blue line are closer to the ideal rock-salt geometry, whereas those near the red line deviate most strongly.

A global comparison of the angle deviations shows that, although Te has the highest MAD of ≈13°, the spread around this mean is relatively narrow. This indicates a uniformly disordered Te environment, which has been reported to promote higher SPTC compared to more localized disorder, as seen in amorphous Si [13] and in the contrast between vacancy and Frenkel defects in crystalline W [49]. For Ge, the element-level conductivity is correlated with angular disorder: κ_{Ge} is lowest in M7, which exhibits the largest MAD, and highest in M10, which shows the smallest MAD. By contrast, the SPTC of Sb appears largely insensitive to angular deviations, consistent with its mean angle remaining close to the ideal rock-salt value.

This ordering is physically consistent with the established picture of heat transport in aGST. At room temperature, thermal conduction is dominated by diffuson-like vibrational modes rather than well-defined propagating phonons; in the Allen–Feldman framework [50,51], the SPTC depends on both the vibrational density of states (VDOS) in the mid- to low-frequency window and Ξ. Figure S6 illustrates this clearly: Te and Sb contribute disproportionately in the low–mid frequency range where diffuson-like modes dominate amorphous transport.

The relative contributions of the three vibrational regimes—propagons, diffusons, and locons—following the definitions of Allen and Feldman [50,51] can be analyzed by computing the thermal diffusivity, refer to Figure S7(b–c). The localized vibrational modes (locons), corresponding to frequencies above 150 cm^{-1}, contribute only marginally to the thermal conductivity, while propagons have an overall contribution that remains limited. The dominant portion of the thermal conductivity arises from the diffuson modes, see Table 3 for the contribution of vibrational regimes to total thermal conductivity for model M5 and 900-atom aGST model.[3]

Within the SPTC formulation, diffuson-like modes contribute to site conductivities through the real-symmetric transport matrix Ξ [13]. In contrast, the VIPR curves (gray lines) associated with Ge peaks in the high-frequency range reveal strong vibrational localization (the locon regime), and such modes contribute little, or nothing, to heat transport [13]. The same VDOS/VIPR pattern is consistently observed across the other eleven models (see Figure S6). An outlier was noted for M9 (localized Ge–Ge stretch modes) in Ref. [53].

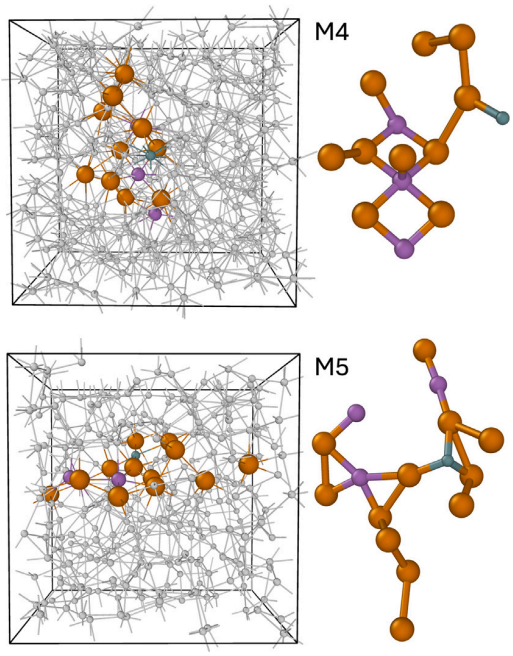

Fig. 7. High SPTC (≥70% of maximum SPTC) filamentary structure in M4 and M5. The atoms are color-coded: teal, purple, and brown for Ge, Sb, and Te, respectively.

We show that the range of the "thermal matrix" Ξ (see Appendix A.3) is ≈8 Å, refer to the Figure S7(a). This quantifies the non-locality of heat transport in aGST. To estimate the site-wise contribution of the thermal conductivity, we require information only within this range.

This same argument for connected, percolative pathways is reinforced by Figs. 6(b) and 7. In Fig. 6(b), SPTC is shown to increase with coordination number (CN) and, more weakly, with mean bond length (BL), with the strongest dependence for Te, intermediate for Sb, and weakest for Ge. These correlations demonstrate that higher coordination and favorable bonding distances provide the structural conditions most conducive to efficient phonon vibration and heat transfer. For per-model comparison, Figure S8 shows the percentage distribution of coordination numbers for the different elements. In addition, the atoms responsible for the top-tier SPTC values (those ≥ 70% of the per-model maximum) form extended filamentary networks. As illustrated for models M4 and M5 in Fig. 7, these space-filling filaments resemble those previously reported in amorphous Si [13] and serve as the primary conduits for thermal transport in aGST.

Two practical observations follow for considerations of materials design. First, the near-universal in-model ranking Te ≥ Sb ≥ Ge suggests that Te-rich (and, to a lesser extent, Sb-rich) regions form the dominant heat-carrying sub-network. For example, in finite-element homogenization, weighting or refining around Te-dense clusters is therefore a sensible strategy when the quantity of interest is the effective conductivity [54,55]. Second, the "sensitivity" of M7 and M10 indicates that modest changes in medium-range order (e.g., a higher fraction of tetrahedral Ge, disrupted Te chains, or enhanced nanoscale porosity) can collectively depress all three site-projected channels, consistent with the sensitivity of amorphous chalcogenides to network topology and vibrational-mode localization.

[3] The boundary between diffusons and locons is the frequency where the vibrational states begin to show significant localization. The diffuson-propagons boundary is estimated at the frequency where the diffusivity begins to fall off toward lower frequencies. It may be preferable to estimate diffusions-propagons boundary from the phase quotient, identifying the frequency at which acoustic-like (high phase quotient) transitions into diffusion modes (low phase quotient) [52].

4. Conclusion

This study provides a novel characterization of amorphous Ge–Sb–Te structures by integrating electronic structure, vibrational analysis, and transport properties. Hybrid-functional calculations (HSE06) and the space-projected conductivity (SPC) reveal the role of mid-gap states, often associated with over-coordinated Ge atoms, in shaping electronic activity and conductivity. Thermally induced electronic fluctuations highlight the strong electron–phonon coupling at room temperature, especially for conduction tail states.

On the thermal side, the site-projected thermal conductivity (SPTC) analysis reveals that Te- and Sb-rich regions form the dominant pathways for heat conduction (even taking into account the higher Te concentration due to the stoichiometry). Extended filamentary and chemically selective networks govern thermal transport in aGST. The SPTC statistics capture a chemically intuitive partitioning of heat flow, consistent with the broader literature on chalcogenides and amorphous vibrational transport.

The combined use of SPC for electrons and SPTC for phonons establishes a framework for mapping charge and heat transport at the atomic scale. This spatially resolved perspective not only explains experimentally observed features, such as the low lattice thermal conductivity and the variability of electronic transport in aGST, but also provides a generalizable methodology for analyzing transport in disordered materials.

CRediT authorship contribution statement

K. Nepal: Writing – review & editing, Writing – original draft, Visualization, Validation, Software, Resources, Methodology, Investigation, Formal analysis, Data curation, Conceptualization. **A. Gautam:** Writing – review & editing, Visualization, Software, Methodology, Investigation, Formal analysis, Conceptualization. **R. Hussein:** Writing – review & editing, Visualization, Software, Resources, Methodology, Investigation. **K. Konstantinou:** Writing – review & editing, Validation, Resources, Investigation, Formal analysis, Data curation, Conceptualization. **S.R. Elliott:** Writing – review & editing, Validation, Resources, Investigation, Formal analysis, Data curation, Conceptualization. **C. Ugwumadu:** Writing – review & editing, Visualization, Validation, Resources, Methodology, Investigation, Formal analysis, Data curation, Conceptualization. **D.A. Drabold:** Writing – review & editing, Validation, Supervision, Resources, Project administration, Methodology, Investigation, Funding acquisition, Formal analysis, Conceptualization.

Funding

The computational resource used in this work was supported by the US National Science Foundation (NSF) under award number MRI2320493 and the Office of Naval Research, United States under grant N000142312773. K. N. acknowledges financial support from the Nanoscale & Quantum Phenomena Institute (NQPI), United States, conferred through the NQPI graduate research fellowship. K.K. acknowledges financial support from the Research Council of Finland under grant no. 364241 (“NoneqRSMSD”). S.R.E. is grateful to the Leverhulme Trust (UK) for a Fellowship. C. U. acknowledges funding from the Laboratory Directed Research and Development program of Los Alamos National Laboratory, United States under the Director’s Postdoctoral Fellowship Program, project number 20240877PRD4. Los Alamos National Laboratory is operated by Triad National Security, LLC, for the National Nuclear Security Administration, United States[http://dx.doi.org/10.13039/100006168] of the U.S. Department of Energy (Contract No. 89233218CNA000001).

Declaration of competing interest

The authors declare that they have no known competing financial interests or personal relationships that could have appeared to influence the work reported in this paper.

Acknowledgment

We gratefully acknowledge Dr. D. Stewart for valuable discussions.

Appendix A. Spatially local estimates of transport

For the atomistic local distribution of conductivity, we computed the space-projected conductivity (SPC), a spatial decomposition of the Kubo–Greenwood formula (KGF) for electronic conductivity, and site-projected thermal conductivity (SPTC)- a spatial decomposition of the Green-Kubo equation for thermal conductivity. The methodology for SPC and SPTC is detailed elsewhere [10–13], but we provide a concise description here.

A.1. Electronic case: Space projected conductivity

Within linear response and the single particle approximation, the average of the diagonal elements of the conductivity tensor for each k-point, $\mathbf{k}$, and frequency, ω, is [18,56]:

$$\sigma_{\mathbf{k}}(\omega) = \frac{2\pi e^2}{3m^2\omega\Omega}\sum_{i,j}\sum_{\alpha}[f(\varepsilon_{i,\mathbf{k}}) - f(\varepsilon_{j,\mathbf{k}})]\times \\ |\langle\psi_{j,\mathbf{k}}|p^{\alpha}|\psi_{i,\mathbf{k}}\rangle|^2\delta(\varepsilon_{j,\mathbf{k}} - \varepsilon_{i,\mathbf{k}} - \hbar\omega) \tag{A.1}$$

where e and m represent the charge and mass of the electron, respectively. Ω represents the volume of the supercell. $\psi_{i,\mathbf{k}}$ is the Kohn–Sham orbital associated with eigenvalue $\varepsilon_{i,\mathbf{k}}$. $f(\varepsilon_{i,\mathbf{k}})$ is the Fermi-Dirac weight and p^{α} is the momentum operator along the Cartesian direction α.

If we define $g_{ij}(\mathbf{k},\omega)$ as

$$g_{ij}(\mathbf{k},\omega) = \frac{2\pi e^2}{3m^2\omega\Omega}[f(\varepsilon_{i,\mathbf{k}}) - f(\varepsilon_{j,\mathbf{k}})]\delta(\varepsilon_{j,\mathbf{k}} - \varepsilon_{i,\mathbf{k}} - \hbar\omega) \tag{A.2}$$

The conductivity can then be expressed as (and dropping the $\mathbf{k}$ and ω dependence):

$$\sigma = \sum_{i,j,\alpha} g_{ij}\int d^3x\int d^3x'[\psi_j^*(x)p^{\alpha}\psi_i(x)][\psi_j^*(x')p^{\alpha}\psi_i(x')]^* \tag{A.3}$$

Taking $\xi_{ji}^{\alpha}(x) = \psi_j^*(x)p^{\alpha}\psi_i(x)$, a complex-valued function defined on a real space grid (call the grid points $\mathbf{x}$) with uniform grid size (h) in three dimensions, then the integrals can be approximated as a sum on the grid from Eq. (A.3) yielding:

$$\sigma \approx h^6\sum_{x,x'}\sum_{i,j,\alpha} g_{ij}\xi_{ji}^{\alpha}(x)(\xi_{ji}^{\alpha}(x'))^* \tag{A.4}$$

In Eq. (A.4), the approximation becomes exact as $h \to 0$. Next, we define a Hermitian positive semi-definite matrix:

$$\Gamma(x,x') = \sum_{i,j,\alpha} g_{ij}\xi_{ji}^{\alpha}(x)[\xi_{ji}^{\alpha}(x')]^* \tag{A.5}$$

The matrix elements of Γ have the dimension of conductivity, and summation over all grid points recovers the KGF conductivity of the system within a limit as $h \to 0$. Summing out x' gives the SPC (ζ) at real-space grid points x.

$$\zeta(x) = \left|\sum_{x'}\Gamma(x,x')\right| \tag{A.6}$$

The modulus is taken to ensure a real value for the scalar field ζ.

In spectral form, we can write:

$$\sigma = \sum_{x}\Gamma(x,x) + \sum_{x,x',x\neq x'}\Gamma(x,x') \tag{A.7}$$

We show elsewhere that the object Γ is interesting. Its eigenvalue problem reads $\Gamma\chi_{\mu} = \Lambda_{\mu}\chi_{\mu}$. Γ always exhibits a huge null space, so that its eigenvectors conjugate to a set of extremal Λ offer a compact representation for the conduction active parts of the network.

The method has been implemented with VASP. It is possible to use a local orbital DFT Hamiltonian as in SIESTA [57] or FIREBALL [58], in which case one could extract site-projected SPC, which might be convenient for large systems.

A.1.1. Electronic conductivity and SPC in aGST

The wave-functions in Eq. (A.1) are the Kohn–Sham orbitals $\Psi_{i;\mathbf{k}}$ computed within VASP. The gradient of ψ_i for each α was computed using the central finite difference method. The partial occupancies of the energy levels near the Fermi level were approximated using the electronic temperature $T = 1000$ K for the Fermi-Dirac distribution. The δ function was approximated using a Gaussian of width 0.04 eV. To implement the SPC method, the 315-atom aGST models were divided into a real space grid of $54 \times 54 \times 54$ ($dim\ \Gamma = 157464$). Refs. [59–62] detail the dependence of KGF conductivity and SPC on different factors involving the KGF formalism.

A.2. Electronic case: N^2method [40]

We next describe a simple and convenient method for both estimating the electrical conductivity of a material and extracting a spatial density function, which provides information about the spatial distribution of electrical conductivity. We have named this the N^2 method [40,49], and tersely recount the derivation here. It follows from the work of Mott [63,64] and Hindley [65,66], which indicates that electronic conductivity (σ) is determined by electronic activity near the Fermi energy (ε_f). In particular, σ is proportional to the square of the electronic density of states ($N(E)$) around ε_f, expressed as [40]:

$$\sigma \propto [N(E)]^2\Big|_{E\to\varepsilon_f} \tag{A.8}$$

This approximation is valid for systems with extended states near ε_f. It is sometimes forgotten in the current literature that $N^2(\varepsilon_f)$, *not* $N(\varepsilon_f)$ is a proxy for electronic conductivity [67].

The contribution of the ith Kohn–Sham orbital (ε_i) to the electronic density of states at ε_f is:

$$N(\varepsilon_f) = \frac{1}{M}\sum_i \delta(\varepsilon_i - \varepsilon_f) \tag{A.9}$$

where M is the dimension of the single-particle Hamiltonian, and in practice, the δ function is approximated by a Gaussian function of a selected smearing width. The spatial projection of the electronic conductivity can be expressed as [40]:

$$\bar{\zeta}(\varepsilon_f, \boldsymbol{r}) = \frac{1}{M^2}\sum_{i,j}\delta(\varepsilon_i - \varepsilon_f)\delta(\varepsilon_j - \varepsilon_f)|\psi_i(\boldsymbol{r})|^2|\psi_j(\boldsymbol{r})|^2\beta_{ij} \tag{A.10a}$$

$$\beta_{ij} = \frac{1}{\int |\psi_i(\boldsymbol{r})|^2|\psi_j(\boldsymbol{r})|^2 d\boldsymbol{r}}. \tag{A.10b}$$

where $|\psi_i(\boldsymbol{r})|^2$ denotes the probability density of the ith Kohn–Sham orbital at the spatial grid point $\boldsymbol{r}$. The quantity β_{ij} ensures that the volume integral of Eq. (A.10) approximates $N^2(\varepsilon_f)$ and $|\psi_i(\boldsymbol{r})|^2|\psi_j(\boldsymbol{r})|^2$ vanishes in grid regions where the wavefunctions do not overlap. Since each grid point $\boldsymbol{r}$ represents a contribution to N^2, their projection thus highlights electronic activity within the system.

A.2.1. Finite-temperature generalization

For a semiconductor, the δ-functions in Eqs. (A.9)–(A.10) should be weighted by the finite-temperature electronic occupations. The contribution to transport is governed by the Fermi–Dirac weighting factor that highlights electronic states that participate at temperature T. Thus, for finite-temperature transport:

$$\delta(\varepsilon_i - \varepsilon_f) \longrightarrow -\frac{\partial f_T(\varepsilon_i)}{\partial \varepsilon_i}. \tag{A.11}$$

This accounts for thermally activated carriers in a semiconductor and reduces to Eqs. (A.9)–(A.10) in the zero-temperature limit.

A.3. Thermal case: site-projected thermal conductivity: SPTC

In a classic paper, Allen and Feldman (AF) worked out thermal transport from the Green-Kubo formula in the harmonic approximation, for disordered systems and a quantized lattice [50,51]. We have explained how to extract SPTC elsewhere [12,13] from their work, and for completeness, tersely repeat it here. At the Γ point of the Brillouin zone, the vibrational normal modes are real. For such a case, the AF expression for TC is:

$$\begin{aligned}\kappa = &\frac{\pi\hbar}{48TV}\sum_{m,n\neq m}\left[-\frac{\partial\langle f_m\rangle}{\partial\omega_m}\right]\delta(\omega_m-\omega_n)\frac{(\omega_m+\omega_n)^2}{\omega_m\omega_n}\\ &\sum_\eta\sum_{\alpha,\beta}\sum_{\gamma,x,x'} e_x^{\alpha m}e_{x'}^{\beta n}\frac{1}{\sqrt{m_x m_{x'}}}\phi_{xx'}^{\alpha\beta}(0,\gamma)\left(R_\gamma^\eta + R_{xx'}^\eta\right)\\ &\sum_{\alpha',\beta'}\sum_{\gamma',a,b} e_a^{\alpha' m}e_b^{\beta' n}\frac{1}{\sqrt{m_a m_b}}\phi_{ab}^{\alpha'\beta'}(0,\gamma')\left(R_{\gamma'}^\eta + R_{ab}^\eta\right)\end{aligned} \tag{A.12}$$

where, m and n are the indices of the classical normal modes, f_m is the equilibrium occupation of the mth mode, ω_m and $e_i^{\alpha m}$ are the vibrational frequency $\omega_m^{\mathbf{0}}$ and the polarization $e_{i\mathbf{0}}^{\alpha m}$. R_γ^η is the ηth component of $\mathbf{R}_\gamma$; $R_{xx'}^\eta$ is the ηth component of $\mathbf{R}_{xx'}$. Also, $\phi_{xx'}^{\alpha\beta}$ is the force constant tensor. The thermal conductivity in Eq. (A.12), is taken as an average of the diagonal components of the conductivity tensor.

The AF form for TC may be rearranged as a double sum over spatial points (labeled x). Carrying this out, with Eq. (A.12), we find:

$$\kappa = \sum_{x,x'}\Xi(x,x'), \tag{A.13}$$

where

$$\begin{aligned}\Xi(x,x') = &\frac{\pi\hbar^2}{48k_BT^2V}\frac{1}{\sqrt{m_{x'}m_x}}\sum_\eta\sum_\gamma\left(R_\gamma^\eta + R_{xx'}^\eta\right)\sum_{m,n\neq m}\delta(\omega_m-\omega_n)\\ &\frac{(\omega_m+\omega_n)^2}{\omega_m\omega_n}\left(\frac{e^{\frac{\hbar\omega_m}{k_BT}}}{\left(e^{\frac{\hbar\omega_m}{k_BT}}-1\right)^2}\right)\sum_{\alpha\beta}\phi_{x,x'}^{\alpha\beta}(0,\gamma)e_x^{\alpha m}e_{x'}^{\beta n}\\ &\sum_{\gamma' ab}\sum_{\alpha'\beta'}\frac{1}{\sqrt{m_a m_b}}\phi_{a,b}^{\alpha'\beta'}(0,\gamma')e_a^{\alpha' m}e_b^{\beta' n}\left(R_{\gamma'}^\eta + R_{ab}^\eta\right).\end{aligned} \tag{A.14}$$

Ξ is called the "thermal matrix". It is a real-symmetric matrix with units of thermal conductivity. A Lorentzian function approximates the δ function. We decompose the total TC into contributions depending on atomic position x by summing out one index of $\Xi(x,x')$ over positions x':

$$\zeta(x) = \sum_{x'}\Xi(x,x'). \tag{A.15}$$

We call $\zeta(x)$ the *site-projected thermal conductivity* (SPTC), the contribution of an atom at site x in a supercell to the total TC of the system, since:

$$\kappa = \sum_x \zeta(x). \tag{A.16}$$

For anisotropic systems or off-diagonal terms, the conductivity tensor $\kappa_{\alpha\beta}$ local contributions can be similarly obtained.

A simple argument clarifies the physical meaning of SPTC. The decomposition above expresses the thermal conductivity as a sum over all pairs of sites. Now, imagine removing one atom from the cell at position y. The difference in thermal conductivity between the original system and the one with the atom missing at y is evidently (by excluding all the terms involving the site y in the SPTC) $\Delta_y = 2\sum_{x'}\Xi(x',y)$ which we can call the "Atomic Removal Conductivity" (ARC) for site y and we used the fact that the thermal matrix, Ξ, is symmetric. The term $\sum_{x'}\Xi(x',y)$ is exactly the SPTC for site y obtained from the preceding discussion, so that $\zeta_\kappa(y) = \Delta_y/2$. *We conclude that the SPTC at site y is just half of the ARC.*

Electrons and phonons both contribute to the thermal conductivity in aGST, but we will limit ourselves to the lattice contribution (phonons). A cutoff distance of $r_c = 8$ Å was used for the calculation based on SPTC convergence shown in Figure S7a.

A.3.1. Discussion on thermal conductivity and broadening factor in aGST

Refs. [12,13] detail the dependence of thermal conductivity on different factors involving the SPTC formalism. Thermal conductivity significantly depends on the broadening factor (δ in Eq. (A.14)). Thermal conductivity increases with increasing broadening factor and remains uniform at smearing window 1.9–2.1 K. In addition, the SPTC per atom remains stable within this smearing window. The thermal conductivity in aGST computed with the 2 K broadening provides values that agree well with the previous theoretical prediction and experimental measurements.

Appendix B. Supplementary data

Supplementary material related to this article can be found online at https://doi.org/10.1016/j.solidstatesciences.2025.108182.

Data availability

Data will be made available on request.

References

[1] J. Hegedüs, S. Elliott, Microscopic origin of the fast crystallization ability of Ge–Sb–Te phase-change memory materials, Nat. Mater. 7 (5) (2008) 399–405, http://dx.doi.org/10.1038/nmat2157.

[2] D. Lencer, M. Salinga, B. Grabowski, T. Hickel, J. Neugebauer, M. Wuttig, A map for phase-change materials, Nat. Mater. 7 (12) (2008) 972–977, http://dx.doi.org/10.1038/nmat2330.

[3] W. Zhang, R. Mazzarello, M. Wuttig, E. Ma, Designing crystallization in phase-change materials for universal memory and neuro-inspired computing, Nat. Rev. Mater. 4 (3) (2019) 150–168, http://dx.doi.org/10.1038/s41578-018-0076-x.

[4] X. Zhou, M. Xia, F. Rao, L. Wu, X. Li, Z. Song, S. Feng, H. Sun, Understanding phase-change behaviors of carbon-doped Ge2Sb2Te5 for phase-change memory application, ACS Appl. Mater. Interfaces 6 (16) (2014) 14207–14214, http://dx.doi.org/10.1021/am503502q.

[5] S. Mukhopadhyay, J. Sun, A. Subedi, T. Siegrist, D.J. Singh, Competing covalent and ionic bonding in Ge–Sb–Te phase change materials, Sci. Rep. 6 (1) (2016) http://dx.doi.org/10.1038/srep25981.

[6] M. Esser, S. Maintz, R. Dronskowski, Automated first-principles mapping for phase-change materials, J. Comput. Chem. 38 (9) (2017) 620–628, http://dx.doi.org/10.1002/jcc.24724.

[7] K. Konstantinou, F.C. Mocanu, T.-H. Lee, S.R. Elliott, Revealing the intrinsic nature of the mid-gap defects in amorphous Ge2Sb2Te5, Nat. Commun. 10 (1) (2019) http://dx.doi.org/10.1038/s41467-019-10980-w.

[8] F.C. Mocanu, K. Konstantinou, S.R. Elliott, Quench-rate and size-dependent behaviour in glassy $Ge_2Sb_2Te_5$ models simulated with a machine-learned Gaussian approximation potential, J. Phys. D: Appl. Phys. 53 (24) (2020) 244002, http://dx.doi.org/10.1088/1361-6463/ab77de.

[9] K. Konstantinou, F.C. Mocanu, J. Akola, Electron localization in recrystallized models of the $Ge_2Sb_2Te_5$ phase-change memory material, Phys. Rev. B 106 (18) (2022) http://dx.doi.org/10.1103/physrevb.106.184103.

[10] K. Prasai, K.N. Subedi, K. Ferris, P. Biswas, D.A. Drabold, Spatial projection of electronic conductivity: The example of conducting bridge memory materials, Phys. Status Solidi (RRL) – Rapid Res. Lett. 12 (9) (2018) 1800238, http://dx.doi.org/10.1002/pssr.201800238.

[11] K.N. Subedi, K. Prasai, D.A. Drabold, Space-projected conductivity and spectral properties of the conduction matrix, Phys. Status Solidi (B) 258 (9) (2021) 2000438, http://dx.doi.org/10.1002/pssb.202000438.

[12] A. Gautam, Y.G. Lee, C. Ugwumadu, K. Nepal, S. Nakhmanson, D.A. Drabold, Site-projected thermal conductivity: Application to defects, interfaces, and homogeneously disordered materials, Phys. Status Solidi (RRL) – Rapid Res. Lett. 19 (2) (2024) http://dx.doi.org/10.1002/pssr.202400306.

[13] C. Ugwumadu, A. Gautam, Y.G. Lee, D.A. Drabold, Mapping thermal conductivity at the atomic scale: A step toward the thermal design of materials, Phys. Status Solidi (B) (2025) http://dx.doi.org/10.1002/pssb.202500316.

[14] G. Kresse, J. Hafner, Ab initio molecular dynamics for liquid metals, Phys. Rev. B 47 (1993) 558–561, http://dx.doi.org/10.1103/PhysRevB.47.558.

[15] A.P. Thompson, H.M. Aktulga, R. Berger, D.S. Bolintineanu, W.M. Brown, P.S. Crozier, P.J. in 't Veld, A. Kohlmeyer, S.G. Moore, T.D. Nguyen, R. Shan, M.J. Stevens, J. Tranchida, C. Trott, S.J. Plimpton, LAMMPS - a flexible simulation tool for particle-based materials modeling at the atomic, meso, and continuum scales, Comput. Phys. Comm. 271 (2022) 108171, http://dx.doi.org/10.1016/j.cpc.2021.108171.

[16] F.C. Mocanu, K. Konstantinou, T.H. Lee, N. Bernstein, V.L. Deringer, G. Csányi, S.R. Elliott, Modeling the phase-change memory material, $Ge_2Sb_2Te_5$, with a machine-learned interatomic potential, J. Phys. Chem. B 122 (38) (2018) 8998–9006, http://dx.doi.org/10.1021/acs.jpcb.8b06476.

[17] J. Heyd, G.E. Scuseria, M. Ernzerhof, Hybrid functionals based on a screened Coulomb potential, J. Chem. Phys. 118 (18) (2003) 8207–8215, http://dx.doi.org/10.1063/1.1564060.

[18] R. Kubo, Statistical-mechanical theory of irreversible processes. I. General theory and simple applications to magnetic and conduction problems, J. Phys. Soc. Japan 12 (6) (1957) 570–586, http://dx.doi.org/10.1143/JPSJ.12.570.

[19] M.S. Green, Markoff random processes and the statistical mechanics of time-dependent phenomena. II. Irreversible processes in fluids, J. Chem. Phys. 22 (3) (1954) 398–413, http://dx.doi.org/10.1063/1.1740082.

[20] T.H. Lee, S.R. Elliott, Multi-center hyperbonding in phase-change materials, Phys. Status Solidi (RRL) – Rapid Res. Lett. 15 (3) (2021) http://dx.doi.org/10.1002/pssr.202000516.

[21] M. Xu, Y.Q. Cheng, H.W. Sheng, E. Ma, Nature of atomic bonding and atomic structure in the phase-change $Ge_2Sb_2Te_5$ Glass, Phys. Rev. Lett. 103 (19) (2009) http://dx.doi.org/10.1103/physrevlett.103.195502.

[22] S. Caravati, M. Bernasconi, T.D. Kühne, M. Krack, M. Parrinello, First-principles study of crystalline and amorphous Ge2Sb2Te5and the effects of stoichiometric defects, J. Phys.: Condens. Matter. 21 (25) (2009) 255501, http://dx.doi.org/10.1088/0953-8984/21/25/255501.

[23] B.-S. Lee, J.R. Abelson, S.G. Bishop, D.-H. Kang, B.-k. Cheong, K.-B. Kim, Investigation of the optical and electronic properties of Ge2Sb2Te5 phase change material in its amorphous, cubic, and hexagonal phases, J. Appl. Phys. 97 (9) (2005) http://dx.doi.org/10.1063/1.1884248.

[24] T. Kato, K. Tanaka, Electronic properties of amorphous and crystalline Ge2Sb2Te5 films, Japan. J. Appl. Phys. 44 (10R) (2005) 7340, http://dx.doi.org/10.1143/jjap.44.7340.

[25] R. Nelson, C. Ertural, J. George, V.L. Deringer, G. Hautier, R. Dronskowski, LOBSTER: Local orbital projections, atomic charges, and chemical-bonding analysis from projector-augmented-wave-based density-functional theory, J. Comput. Chem. 41 (21) (2020) 1931–1940, http://dx.doi.org/10.1002/jcc.26353.

[26] K. Konstantinou, S.R. Elliott, J. Akola, Inherent electron and hole trapping in amorphous phase-change memory materials: $Ge_2Sb_2Te_5$, J. Mater. Chem. C 10 (17) (2022) 6744–6753, http://dx.doi.org/10.1039/d2tc00486k.

[27] J. Luckas, D. Krebs, S. Grothe, J. Klomfaß, R. Carius, C. Longeaud, M. Wuttig, Defects in amorphous phase-change materials, J. Mater. Res. 28 (9) (2013) 1139–1147, http://dx.doi.org/10.1557/jmr.2013.72.

[28] R. Atta-Fynn, P. Biswas, D.A. Drabold, Electron–phonon coupling is large for localized states, Phys. Rev. B 69 (24) (2004) http://dx.doi.org/10.1103/physrevb.69.245204.

[29] K. Prasai, P. Biswas, D.A. Drabold, Electrons and phonons in amorphous semiconductors, Semicond. Sci. Technol. 31 (7) (2016) 073002, http://dx.doi.org/10.1088/0268-1242/31/7/073002.

[30] H. Overhof, P. Thomas, Electronic Transport in Hydrogenated Amorphous Silicon, in: Springer Tracts in Modern Physics, vol. 114, Springer, Berlin, 1989.

[31] P. Thomas, Insulating and semiconducting glasses, in: P. Boolchand (Ed.), Insulating and Semiconducting Glasses, World Scientific, Singapore, 2000, p. 553.

[32] J. Li, D.A. Drabold, Electron hopping between localized states: A simulation of the finite-temperature Anderson problem using density functional methods, Phys. Rev. B 68 (3) (2003) http://dx.doi.org/10.1103/physrevb.68.033103.

[33] T.A. Abtew, D.A. Drabold, Thermally driven hopping and electron transport in amorphous materials from density functional calculations, J. Phys.: Condens. Matter. 16 (44) (2004) S5289, http://dx.doi.org/10.1088/0953-8984/16/44/025.

[34] T.A. Abtew, M. Zhang, D.A. Drabold, Ab initioestimate of temperature dependence of electrical conductivity in a model amorphous material: Hydrogenated amorphous silicon, Phys. Rev. B 76 (4) (2007) http://dx.doi.org/10.1103/physrevb.76.045212.

[35] D.A. Drabold, P.A. Fedders, Electronic consequences of the mutual presence of thermal and structural disorder, Phys. Rev. B 60 (2) (1999) R721–R725, http://dx.doi.org/10.1103/physrevb.60.r721.

[36] S. Nosé, A unified formulation of the constant temperature molecular dynamics methods, J. Chem. Phys. 81 (1) (1984) 511–519, http://dx.doi.org/10.1063/1.447334.

[37] W.G. Hoover, Canonical dynamics: Equilibrium phase-space distributions, Phys. Rev. A 31 (3) (1985) 1695–1697, http://dx.doi.org/10.1103/physreva.31.1695.

[38] D.A. Drabold, P.A. Fedders, S. Klemm, O.F. Sankey, Finite-temperature properties of amorphous silicon, Phys. Rev. Lett. 67 (16) (1991) 2179–2182, http://dx.doi.org/10.1103/physrevlett.67.2179.

[39] S. Aljishi, J.D. Cohen, S. Jin, L. Ley, Band tails in hydrogenated amorphous silicon and silicon-germanium alloys, Phys. Rev. Lett. 64 (1990) 2811–2814, http://dx.doi.org/10.1103/PhysRevLett.64.2811.

[40] K. Nepal, C. Ugwumadu, F. Kraft, Y. Al-Majali, D. Drabold, The effects of crystal orientation and common coal impurities on electronic conductivity in copper–carbon composites, Carbon 231 (2025) 119711, http://dx.doi.org/10.1016/j.carbon.2024.119711.

[41] C. Ma, J. He, J. Lu, J. Zhu, Z. Hu, Modeling of the temperature profiles and thermoelectric effects in phase change memory cells, Appl. Sci. 8 (8) (2018) 1238, http://dx.doi.org/10.3390/app8081238.
[42] K. Aryana, D.A. Stewart, J.T. Gaskins, J. Nag, J.C. Read, D.H. Olson, M.K. Grobis, P.E. Hopkins, Tuning network topology and vibrational mode localization to achieve ultralow thermal conductivity in amorphous chalcogenides, Nat. Commun. 12 (1) (2021) 2817.
[43] J. Moon, A.J. Minnich, Sub-amorphous thermal conductivity in amorphous heterogeneous nanocomposites, RSC Adv. 6 (2016) 105154–105160, http://dx.doi.org/10.1039/C6RA24053D.
[44] Q. Li, O. Levit, E. Yalon, B. Sun, Temperature-dependent thermal conductivity of $Ge_2Sb_2Te_5$ polymorphs from 80 to 500K, J. Appl. Phys. 133 (13) (2023) http://dx.doi.org/10.1063/5.0142536.
[45] F.C. Mocanu, K. Konstantinou, S.R. Elliott, Nonequilibrium ab initio molecular-dynamics simulations of lattice thermal conductivity in irradiated glassy Ge2Sb2Te5, Appl. Phys. Lett. 116 (3) (2020) http://dx.doi.org/10.1063/1.5132962.
[46] L. Yang, B.-Y. Cao, Thermal transport of amorphous phase change memory materials using population-coherence theory: a first-principles study, J. Phys. D: Appl. Phys. 54 (50) (2021) 505302, http://dx.doi.org/10.1088/1361-6463/ac1ec3.
[47] Z. Sun, J. Zhou, R. Ahuja, Structure of phase change materials for data storage, Phys. Rev. Lett. 96 (2006) 055507, http://dx.doi.org/10.1103/PhysRevLett.96.055507.
[48] H. Cinkaya, A. Ozturk, A. Sirri Atilla Hasekioğlu, Z. Evren Kaya, S. Kalem, C. Charpin-Nicolle, G. Bourgeois, N. Guillaume, M.C. Cyrille, J. Garrione, G. Navarro, E. Nowak, Structural properties of Ge–Sb–Te alloys, Solid-State Electron. 185 (2021) 108101, http://dx.doi.org/10.1016/j.sse.2021.108101.
[49] C. Ugwumadu, D.A. Drabold, R.M. Tutchton, Effects of galactic irradiation on thermal and electronic transport in tungsten, Phys. Status Solidi (B) 2500109, http://dx.doi.org/10.1002/pssb.202500109.
[50] P.B. Allen, J.L. Feldman, Thermal conductivity of disordered harmonic solids, Phys. Rev. B 48 (1993) 12581–12588, http://dx.doi.org/10.1103/PhysRevB.48.12581.
[51] P.B. Allen, J.L. Feldman, J. Fabian, F. Wooten, Diffusons, locons and propagons: Character of atomic vibrations in amorphous Si, Philos. Mag. B 79 (11–12) (1999) 1715–1731, http://dx.doi.org/10.1080/13642819908223054.
[52] C. Ugwumadu, K. Subedi, R. Thapa, P. Apsangi, S. Swain, M. Kozicki, D. Drabold, Structure, vibrations and electronic transport in silicon suboxides: Application to physical unclonable functions, J. Non-Crystalline Solids: X 18 (2023) 100179, http://dx.doi.org/10.1016/j.nocx.2023.100179.
[53] Animation of bond stretching modes in GST. URL http://people.ohio.edu/drabold/GST/. Materials Theory Group (MTG), Ohio University.
[54] R.W. Lewis, K. Morgan, H. Thomas, K.N. Seetharamu, The Finite Element Method in Heat Transfer Analysis, first ed., John Wiley & Sons, 1996.
[55] W. Tian, L. Qi, X. Chao, J. Liang, M. Fu, Numerical evaluation on the effective thermal conductivity of the composites with discontinuous inclusions: Periodic boundary condition and its numerical algorithm, Int. J. Heat Mass Transfer 134 (2019) 735–751, http://dx.doi.org/10.1016/j.ijheatmasstransfer.2019.01.072.
[56] D.A. Greenwood, The Boltzmann equation in the theory of electrical conduction in metals, Proc. Phys. Soc. 71 (4) (1958) 585–596, http://dx.doi.org/10.1088/0370-1328/71/4/306.
[57] J.M. Soler, E. Artacho, J.D. Gale, A. García, J. Junquera, P. Ordejón, D. Sánchez-Portal, The SIESTA method for *ab initio* materials simulation, J. Phys.: Condens. Matter. 14 (11) (2002) 2745–2779, http://dx.doi.org/10.1088/0953-8984/14/11/302.
[58] J.P. Lewis, P. Jelínek, J. Ortega, A.A. Demkov, D.G. Trabada, B. Haycock, H. Wang, G. Adams, J.K. Tomfohr, E. Abad, H. Wang, D.A. Drabold, Advances and applications in the FIREBALL ab initio tight-binding molecular-dynamics formalism, Phys. Status Solidi (B) 248 (9) (2011) 1989–2007, http://dx.doi.org/10.1002/pssb.201147259.
[59] D. Knyazev, P. Levashov, Ab initio calculation of transport and optical properties of aluminum: Influence of simulation parameters, Comput. Mater. Sci. 79 (2013) 817–829, http://dx.doi.org/10.1016/j.commatsci.2013.04.066.
[60] L. Calderín, V. Karasiev, S. Trickey, Kubo–Greenwood electrical conductivity formulation and implementation for projector augmented wave datasets, Comput. Phys. Comm. 221 (2017) 118–142, http://dx.doi.org/10.1016/j.cpc.2017.08.008.
[61] P. Bulanchuk, On the delta function broadening in the Kubo–Greenwood equation, Comput. Phys. Comm. 261 (2021) 107714, http://dx.doi.org/10.1016/j.cpc.2020.107714.
[62] K.N. Subedi, K. Kappagantula, F. Kraft, A. Nittala, D.A. Drabold, Electrical conduction processes in aluminum: Defects and phonons, Phys. Rev. B 105 (2022) 104114, http://dx.doi.org/10.1103/PhysRevB.105.104114.
[63] N.F. Mott, E.A. Davis, Theory of electrons in a non-crystalline medium, in: Electronic Processes in Non-Crystalline Materials, second ed., Clarendon/Oxford University Press, Oxford, New York, 1979, pp. 11–15, (Chapter 2).
[64] N.F. Mott, Conduction in non-crystalline materials: III. Localized states in a pseudogap and near extremities of conduction and valence bands, Phil. Mag. 19 (160) (1969) 835–852, http://dx.doi.org/10.1080/14786436908216338.
[65] N.K. Hindley, Random phase model of amorphous semiconductors I. Transport and optical properties, J. Non-Cryst. Solids 5 (1) (1970) 17–30, http://dx.doi.org/10.1016/0022-3093(70)90193-6.
[66] N.K. Hindley, Random phase model of amorphous semiconductors II. Hot electrons, J. Non-Cryst. Solids 5 (1) (1970) 31–40, http://dx.doi.org/10.1016/0022-3093(70)90194-8.
[67] V.L. Deringer, N. Bernstein, G. Csányi, C. Ben Mahmoud, M. Ceriotti, M. Wilson, D.A. Drabold, S.R. Elliott, Origins of structural and electronic transitions in disordered silicon, Nature 589 (7840) (2021) 59–64, http://dx.doi.org/10.1038/s41586-020-03072-z.